

Ab initio Simulations of EMI–BF₄ Neutral-Surface Interactions in Electrospray Thrusters

N. Laws¹ and E. Petro¹

Sibley School of Mechanical & Aerospace Engineering, Cornell University, Ithaca, New York

(*Electronic mail: nrl49@cornell.edu)

(Dated: 24 December 2025)

Electrospray thrusters promise compact, high specific impulse propulsion for small spacecraft, yet ground characterization remains confounded by secondary species emission and incomplete diagnostics of neutral products. To address these limitations, we perform energy-resolved mixed quantum/classical (QM/MM) *ab initio* molecular dynamics (MD) of neutral 1-ethyl-3-methylimidazolium tetrafluoroborate, EMI–BF₄, colliding with Au extractor surfaces with impact energies from 10 to 100 eV to resolve fragment species spectra, charge states, kinetic energy partitioning, and scattering geometry. The simulations reveal a three-stage sequence with impact energy: the low energy regime, 10 to 20 eV, which favors ionic dissociation, intermediate energy regime, between 30 to 40 eV, opens a neutralization window, and high energy regime, greater than 50 eV, drives covalent fragmentation into many light products with mixed charge states. Fractional energy distributions show a transition from few-body, energy-concentrated outcomes in the low energy regime to many-body, energy-dispersed outcomes in the high energy regime. Deflection angle distributions exhibit a strong mass-to-angle anti-correlation such that heavier fragments favor small deflection, whereas lighter fragments populate larger deflection angles. The fraction of transient metastables peaks near 50 eV, coinciding with abundant neutral fragment production. Importantly, neutral bombardment still produces charged secondaries at the target even when the upstream ion plume is fully suppressed by a decelerating electrode. These findings provide a basis for de-biasing facility measurements by pairing tandem time-of-flight secondary ion mass spectrometry and residual gas analyzer with suppression-bias corrections to inform the design of electrospray thrusters that reduce interception and contamination on extractor surfaces.

NOMENCLATURE

n = Cluster solvation number
 Δt = Maximum microcanonical ensemble timestep
 KE_i = Prescribed incident projectile kinetic energy
 v_{CoM} = Center-of-mass speed
 M = Molar mass
 m = Incident projectile mass
 N_A = Avogadro's constant
 V_0 = Initial orientation vector
 V_i = Target orientation vector
 u = Rotation axis direction
 k_d = Unit rotation axis direction
 θ = Rotation angle between V_0 and V_i
 R = Rotation matrix about k
 K = Skew-symmetric cross-product matrix of k
 δE_{max} = Maximum relative deviation of the total energy
 $E_{tot,i}$ = Instantaneous total energy at MD step i
 $\langle E_{tot} \rangle$ = Time average of the total energy
 ϕ_x, ϕ_y, ϕ_z = Projectile orientation Euler angles
 $\chi_\mu(r_e)$ = Contracted Gaussian-type basis functions
 μ = Atomic center
 r_e = Electron position
 k_p = Primitive Gaussian function index
 $d_{\mu k}$ = Contraction coefficients
 α_k = Primitive exponents
 R_μ = Nuclear position
 E_{XC} = Exchange correlation energy
 ω = Range-separation parameter

$E_X^{HF,LR}(\omega)$ = Long-range Hartree-Fock exchange
 $E_X^{GGA,LR}(\omega)$ = Long-range semilocal GGA exchange
 $E_X^{GGA,SR}(\omega)$ = Short-range semilocal GGA exchange
 $E_C^{GGA,LR}(\omega)$ = Long-range semilocal GGA correlation
 $E_C^{GGA,SR}(\omega)$ = Short-range semilocal GGA correlation
 E_C^{GGA} = Semilocal GGA correlation
 E_C^{NL} = Nonlocal correlation
 a = Exact-exchange mixing parameter
 U_{ij} = Exact-exchange mixing parameter
 r_{LJ} = Interatomic separation
 ϵ = Well depth
 σ = Cutoff parameters
 k_0 = Initial NVE trajectory frame index
 k = NVE trajectory frame index
 N = Number of atoms in a neutral projectile
 $r_i^{(k)}$ = Position vector of atom i at frame k
 $d_{ij}^{(k)}$ = Interatomic distance matrix at frame k
 d_b = Distance threshold defining bond adjacency
 $A_{ij}^{(k)}$ = Bond adjacency matrix
 $G^{(k)}$ = Undirected graph at frame k
 $C^{(k)}$ = Number of connected atoms in $G^{(k)}$
 k_{frag} = NVE trajectory fragmentation frame index
 q_A = Fitted partial charge on atom A
 w_i = Weight for grid point i
 V_i^{QM} = Electrostatic potential at grid point i
 r_{A_i} = Distance from atom A to grid point i
 λ_A = Restraint coefficient applied to atom A
 q_A^0 = Target charge for atom A

$$Q_k(t) = \text{Fragment net charge at time } t$$

ACRONYMS

IL	= Ionic liquid
SSE	= Secondary species emission
SEE	= Secondary electron emission
SIE	= Secondary ion emission
TOF	= Time-of-flight
SIMS	= Secondary ion mass spectrometry
QCM	= Quartz crystal microbalance
RGA	= Residual gas analyzer
MD	= Molecular dynamics
LJ	= Lennard-Jones
EAM	= Embedded atom method
PIR	= Pure ion regime
CEX	= Charge exchange
QM/MM	= Quantum mechanics/molecular mechanics
GAPW	= Gaussian augmented plane wave
DFT	= Density functional theory
QM	= Quantum mechanics
GGA	= Generalized gradient approximation
ADMM-Q	= Auxiliary density matrix method
MM	= Molecular mechanics
RESP	= Restrained electrostatic potential
RMSE	= Root mean square error
RRMSE	= Relative root mean square error
RPA	= Retarding potential analyzer

I. INTRODUCTION

Propulsion systems for miniaturized satellites are often limited by mass, efficiency and lifetime in long-term missions. Electrospray thrusters mitigate the constraints at this scale with compact hardware, high propellant efficiency, and no moving parts. In these devices, capillary action feeds room-temperature ionic liquid (IL) propellants such as 1-ethyl-3-methylimidazolium tetrafluoroborate (EMI-BF₄)¹ to a series of porous emitters. A strong field between the emitters and a shared extractor electrode deforms the IL meniscus at each emitter into a Taylor cone. The field enables ion emission from the IL through the extractor aperture, yielding specific impulses between 100 to 10000 s depending on emission mode and operating point².

A. Propellant Overspray and Extractor Grid Lifetime

Propellant overspray onto the extractor and accelerator grids is regarded as the primary lifetime and ground characterization limitation in electrospray thrusters^{3,4}. Secondary species emission (SSE) leads to the accumulation of backspray material on mission-critical hardware that can distort field lines, increase beam divergence, and trigger electrical

shorts that reduce performance and lifetime⁵. Off-axis particles that collide with the extractor or vacuum chamber surfaces provoke SSE, including electrons, ions, ion clusters, and droplets.

Electrospray ion sources operated in the pure ion regime (PIR) predominantly emit singly charged ions with low solvation number $n < 3$. In this mode, a high electric field localized at the meniscus near the emitter apex drives ion evaporation from room temperature IL's such as EMI–BF₄. By reversing the applied polarity, the dominant charged species produced is changed from beams of cations, such as EMI⁺, in the positive mode or anions, such as BF₄⁻, in the negative mode without changing the underlying evaporation mechanism. Apex fields required for ion evaporation are on the order of 10⁹ V/m⁶, consistent with electrically assisted ion evaporation from an IL meniscus⁷. The emitted species are indexed by the solvation number n , which counts the number of neutral EMI–BF₄ pairs bound to a central ion. Particles with $n = 0$ are monomers, $n = 1$ are dimers, $n = 2$ are trimers, and so forth for larger ion clusters. Because charge-to-mass ratio decreases with $n^{5.8-10}$, the low n ions and clusters set the baseline for propulsive performance and define the species most likely to intercept metallic surfaces. After emission, ions are accelerated roughly through the source potential between the emitter and extractor and then exit with a finite angular spread beyond the grid aperture. Multiscale plume models¹¹⁻¹³ and array experiments^{5,14,15} show that the number and distribution of active emission sites influence beam divergence and the fraction of current intercepted by nearby hardware. As the plume propagates, intra-plume processes provoke fragmentation that populate the plume with neutrals spanning energies from thermal to nearly the full beam potential^{3,16-18}. Therefore, linking plume physics to extractor grid lifetime requires understanding of what species are produced when IL constituents collide with metallic surfaces.

B. Facility Effects and Secondary Species Diagnostics

Unlike in on-orbit operation, vacuum-chamber experimental characterization inherently intercepts the plume on beam targets, diagnostics, and chamber walls, making plume-surface interactions and SSE an unavoidable facility effect. Neutrals formed upstream of the target are not influenced by electrostatic biases, instead they retain the velocity of the parent ion cluster at the moment of breakup and can collide with nearby hardware and chamber surfaces at thermal velocity to full potential. SSE from surfaces impacted by electrospray plumes is measured with experimental diagnostics that separately access charged and neutral products. Uchizono et al. quantifies SSE as a first-order facility effect for electrospray thrusters and must be explicitly characterized during ground testing¹⁹. Uchizono place the onset of secondary electron emission (SEE) near 0.44 eV/u and of secondary ion emission (SIE) near 1 eV/u for IL monomers and small clusters. Uchizono frames these metrics as motivation for the use of instrumentation that can resolve composition, polarity, and energy dependencies of the emitted secondary species.

Time-of-flight secondary ion mass spectrometry (TOF-SIMS) is an experimental instrument that has recently been applied to directly measure charged electrospray ion plume secondaries emitted from beam targets. The instrument directly resolves the mass-to-charge composition of charged secondary species produced when an ion-mode plume impinges on metallic targets representative of grid materials^{20,21}, including surfaces that can become conditioned by deposited propellant during operation²². In these measurements, molecular ion clusters and co-streaming neutrals fragment upon collision with surfaces generating SSE observed in both polarities and include sputtered target ions as well as IL fragments such as B⁺, H⁺, CH₂⁺, F⁻, HF⁻, and BF₄⁻²⁰⁻²². However, TOF-SIMS is intrinsically limited to secondary ions and records positive-ion and negative-ion spectra in separate modes, indicating the need for complete polarity-resolved measurement of propellant-surface fragments.

To understand plume deposition, quartz crystal microbalances (QCM's) have been used. Geiger et al. exposed a 6 MHz QCM to varying impact energy EMI–BF₄ plumes to show that the transition between deposition and sputtering occurs with increasing energy¹⁷, which provides the impact energy threshold to near onset and Au sputtering of 10 to 100 eV targeted in this work. Furthermore, Geiger measured emission of charged secondaries from EMI–BF₄ plumes where the ion plume was electrostatically suppressed so that only neutrals reach the target²⁰. Geiger demonstrated that charged secondaries were produced when neutrals impacted the surface, which implies that neutral impact channels are an important consideration in SSE.

Residual gas analyzer (RGA) complements these charged particle diagnostics by sampling neutrals in situ via electron impact ionization in the analyzer volume. During EMI–BF₄ operation, Shaik et al. used an RGA to identify abundant neutral byproducts¹⁸ such as HF, H₂, and BF, which provides constraints on volatile collision products that are invisible to TOF-SIMS and not separable by suppression-bias probes. The diagnostics discussed establish that, in the thermal to thousands of eV regime characteristic of IL neutrals, neutral incidence with metallic target collisions molecular secondaries.

C. Computational Modeling of Electrospray Surface Collisions

MD simulations have been used to model propellant-surface interactions at the atomic scale. Prior studies by Takahashi et al.²³ and Saiz et al.²⁴ modeled EMI–BF₄ nanodroplets impacting a tungsten surface and crystalline silicon using non-reactive Lennard-Jones (LJ) potentials to model every molecular interaction in the Large-scale Atomic/Molecular Massively Parallel Simulator (LAMMPS)²⁵. These computational models limited the chemical fidelity by excluding bond cleavage, bond formation, and any electronic processes at the metal surface. Saiz indicates that sputtering begins around 12.7 eV per molecule and continues through a collision-cascade phase followed by

thermal evaporation. The sputtering yield increases with impact kinetic energy and, at fixed velocity, decreases with droplet diameter due to backscattering. Saiz establishes energy to sputter yield scaling and ejection pathways for large polyatomic projectiles. In Cidoncha et al., Bendimerad built on this work by employing non-reactive simulations of a single neutral EMI–BF₄ pair impacting a Au slab with a hybrid potential: LJ terms for the projectile IL molecule and an embedded atom method (EAM) potential for Au-Au interactions²⁶. Bendimerad mapped reflection and ionic bond dissociation thresholds across 10 to 90 eV and multiple projectile orientations without explicit modeling of chemical recombination or charge transfer. Recently, Bendimerad et al. extended this work by introducing reactive MD using the reaxFF force field²⁷ to incorporate covalent bond breakage and formation¹⁶ for EMI–BF₄ projectile impacts to Au surfaces between 10 to 1000 eV. Bendimerad reports pseudo-mass spectra and fragmentation channels across impact energies and molecular orientations. Bendimerad notes that neutral EMI–BF₄ covalent fragmentation begins at 10 eV, producing fragments such as BF₂, BF₃, F, and larger IL species. These classical MD approaches clarify kinematics and covalent fragmentation pathways, but do not include explicit electronic degrees of freedom for the incident projectile at the metal surface. As a result, these modeling efforts cannot predict fragment charge state, energy transfer mechanisms, and the recombination of radical species into neutral molecules such as HF and H₂¹⁸ that are central to SSE.

The present work overcomes these limitations by applying mixed quantum/classical (QM/MM) ab initio molecular dynamics (MD) to simulate the charge evolution of neutral EMI–BF₄ impacts on gold extractor surfaces across the 10 to 100 eV kinetic energy window.

II. METHODOLOGY

A. Computational Framework

The charge-resolved collision dynamics of EMI–BF₄ with a gold extractor surface were investigated with CP2K's mixed quantum, classical (QM/MM) module²⁸. CP2K's Quickstep solver and Gaussian and augmented plane wave (GAPW) formulation is leveraged to propagate MD trajectories. CP2K's GAPW module combines localized Gaussian orbitals with uniform plane-wave grids to achieve all-electron accuracy for first-row elements at moderate computational cost. Figure 1 depicts the initial configuration of the simulation cell bounded by 75 × 75 × 75 Å³ vacuum to suppress image interactions in the microcanonical ensemble. The neutral species EMI–BF₄ is geometry optimized as shown in Figure 2, quickly temperature equilibrated to 300 K over 500 fs as depicted in Figure 3 to thermalize the system while retaining the optimized geometry, and is placed 15 Å orthogonally away from the center of a frozen Au slab measuring 16 × 16 × 4 Å³, totaling 2000 atoms. To benchmark and validate the optimized EMI–BF₄ structure used as the incident neutral, key intramolecular metrics are compared against a single-crystal

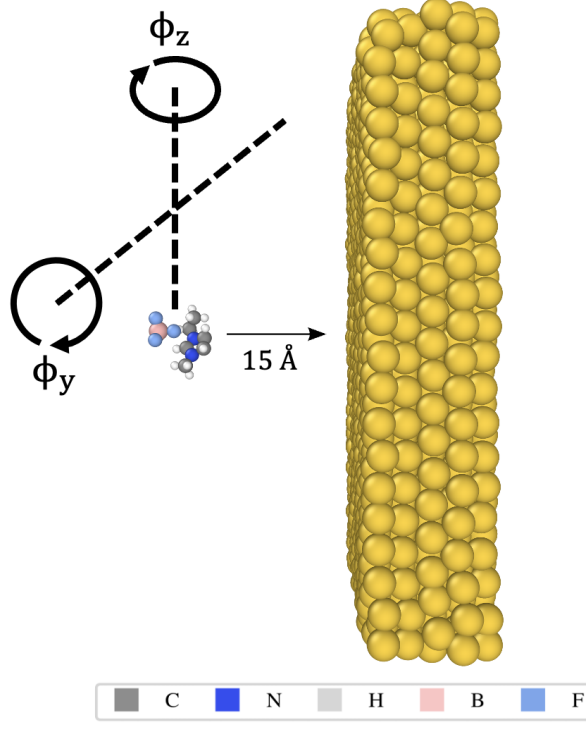


FIG. 1. Simulation domain for extractor surface collisions from incident EMI–BF₄ neutrals.

X-ray structure of EMI–BF₄ collected at 173 K²⁹ as described in Table I. Density functional theory (DFT) optimizations predict three of the four B–F bonds within 0.02 Å of experimental crystallography measurements, whereas one of the B–F bonds is elongated by 0.304 Å. The single elongated B–F likely stems from directional C–H···F bonding from the EMI⁺ cation, which polarizes the BF₄[−] anion toward one F atom and lengthens its attached B–F bond. DFT optimizations calculate the six F–B–F angles to span a broader range in the optimized pair, 94.0 to 123.3°, than the experimental measurements of 108.7 to 111.1°. The imidazolium ring metrics are well reproduced in DFT and are consistent with environmental effects. The isolated contact ion pair optimized in vacuum can relax toward an anisotropic arrangement that strengthens cation to anion contact whereas the solid-state packing of the crystal constrains BF₄[−] closer to tetrahedral geometry. The direct comparison of DFT geometry optimization metrics to experimental crystallography validates the fragmentation pathways upon surface impact.

MD trajectories are propagated in the microcanonical ensemble to a maximum of 2 ps using an adaptive timestep integrator. Integration begins with the timestep $\Delta t = 1$ fs and is recursively halved whenever any atomic displacement exceeds 0.1 Å³⁰. Electrostatics are evaluated with the Martyna–Tuckerman Poisson solver³¹ under fully nonperiodic boundary conditions, eliminating artifacts from spurious periodic images.

In each trajectory, the incident neutral projectile is assigned

TABLE I. Comparison of DFT optimized EMI–BF₄ geometry metrics with experimental crystallography measurements of EMI–BF₄ at 173 K²⁹.

Measurement	DFT	Experimental Crystallography
Anion Bond Lengths (Å)		
B ₁ –F ₁	1.364	1.376
B ₁ –F ₂	1.365	1.386
B ₁ –F ₃	1.378	1.391
B ₁ –F ₄	1.703	1.399
External Anion Angles (°)		
F ₁ –B ₁ –F ₂	94.0	108.7
F ₁ –B ₁ –F ₃	96.0	108.8
F ₁ –B ₁ –F ₄	96.8	109.0
F ₂ –B ₁ –F ₃	113.9	109.5
F ₂ –B ₁ –F ₄	120.0	109.7
F ₃ –B ₁ –F ₄	123.3	111.1
Cation Bond Lengths (Å)		
N ₁ –C ₂	1.292	1.330
C ₂ –N ₃	1.305	1.335
N ₃ –C ₄	1.346	1.361
C ₄ –C ₅	1.436	1.384
C ₅ –N ₁	1.452	1.390
Internal Cation Angles (°)		
C ₅ –N ₁ –C ₂	104.8	106.3
N ₁ –C ₂ –N ₃	106.5	107.8
C ₂ –N ₃ –C ₄	109.2	107.8
N ₃ –C ₄ –C ₅	109.3	108.9
C ₄ –C ₅ –N ₁	110.0	109.3

a translational velocity in the positive \hat{x} direction that reproduces a prescribed center-of-mass kinetic energy, KE_i . For a rigid body of molar mass M , the classical relation

$$v_{CoM} = \sqrt{\frac{2KE_i}{m}} \text{ with } m = \frac{M}{N_A} \quad (1)$$

converts KE_i in J to the laboratory-frame speed v_{CoM} in m/s where N_A is the Avogadro constant. The velocity is subsequently expressed in a_0/t_0 . Only the component orthogonal to the surface normal, \hat{x} , is augmented, thereby isolating impact energy as the sole control parameter.

Atomic coordinates extracted from the equilibrated NVT snapshot are rotated so that the molecular dipole aligns with a target incidence vector V_i . This rotation employs Rodrigues' formula, which converts an axis-angle pair into the rotation matrix

$$R = I + \sin \theta K + (1 - \cos \theta) K^2 \quad (2)$$

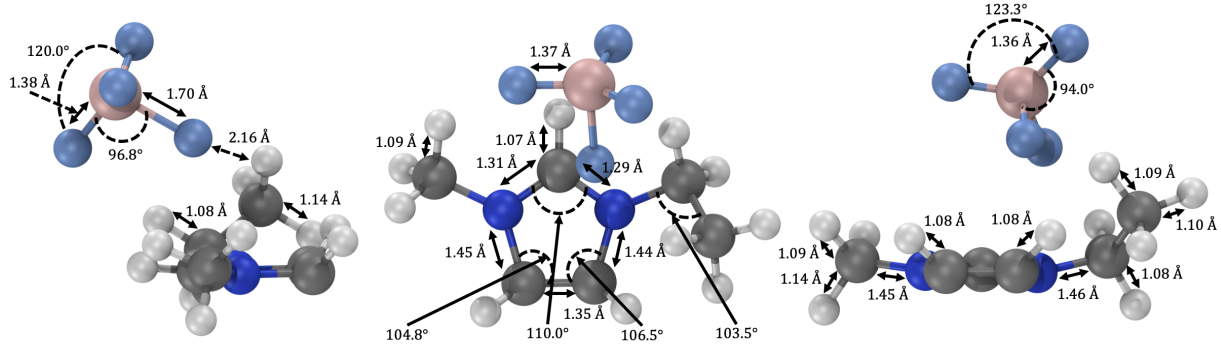
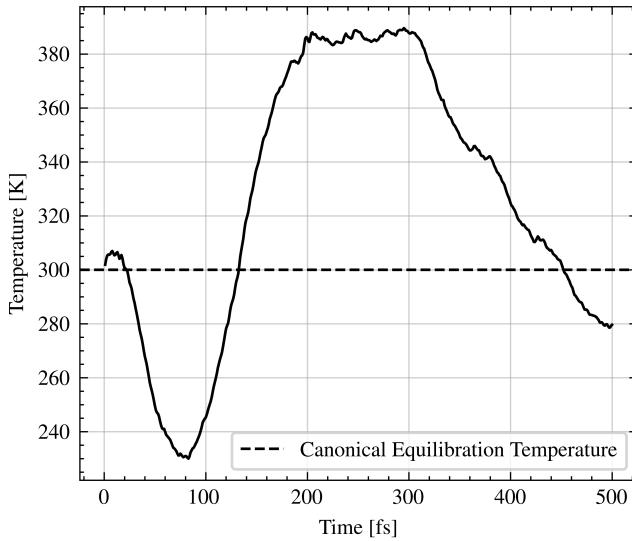
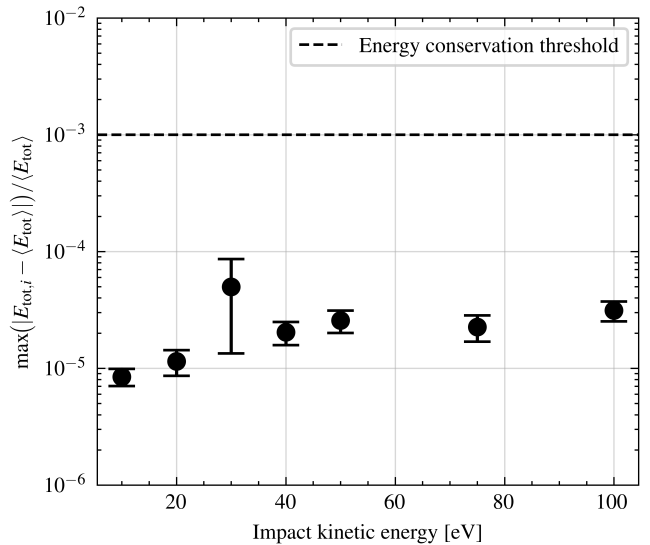
FIG. 2. Molecular geometry of the DFT optimized incident EMI–BF₄ projectile from the right, top, and front views.FIG. 3. Equilibration temperature for the incident EMI–BF₄ neutral during the canonical ensemble.

FIG. 4. Maximum relative deviation of the total energy in microcanonical trajectories across impact kinetic energies.

$$K = \begin{bmatrix} 0 & -k_z & k_y \\ k_z & 0 & -k_x \\ -k_y & k_x & 0 \end{bmatrix} \quad (3)$$

where $k_d = u/\|u\|$ is the unit vector along $u = V_0 \times V_i$ and $\theta = \arccos V_0 \cdot V_i / \|V_0\| \|V_i\|$.

To verify numerical stability and rule out spurious heating in the microcanonical trajectories, the total QM/MM energy, nuclear kinetic, Kohn-Sham electronic, and QM-MM interactions terms, are monitored to ensure conservation. For each trajectory, the worst-case relative energy deviation is computed using Equation 4

$$\delta E_{max} = \frac{\max_i (E_{tot,i} - \langle E_{tot} \rangle)}{\langle E_{tot} \rangle} \quad (4)$$

where $E_{tot,i}$ is the instantaneous total energy at MD step i and $\langle E_{tot} \rangle$ is the time-average over the microcanonical trajectory.

A δE_{max} threshold of 10^{-3} is selected as the acceptance criterion for energy conservation, meaning that values below this boundary indicate that integration error and electronic self-consistency residuals are negligible as compared with energy exchanges on the scale of eV. Figure 4 summarizes δE_{max} as a function of impact kinetic energy. Across the 10 to 100 eV window, all trajectories satisfy the conservation criterion by more than an order of magnitude. The error bars capture the variability across repeated trajectories with different orientations at a given impact kinetic energy.

B. Parameter Space

Energy-resolved tandem mass spectrometry shows that covalent fragmentation of EMI–BF₄ monomers begins at less than 5 eV and reaches full bond cleavage by 35 to 45 eV for gas-phase ions colliding with inert N₂³². The parameter space of this study targets the collision energy window where IL projectiles fragment on impact but do not yet produce signif-

icant sputtering or SEE. Accordingly, prior nonreactive and reactive MD campaigns have confined the simulation domain to a maximum of 100 eV impacts^{16,18}. Guided by these experimental findings, we restrict this study's MD campaign to neutral EMI–BF₄ impacts with Au. The parameter matrix of impact kinetic energies and orientation vectors used to sample the fragmentation kinetics appears in Table II.

TABLE II. Ranges of impact kinetic energy and Euler angles (ϕ_y , ϕ_z) used to initialize each microcanonical trajectory.

Parameter	Min. Value	Max. Value	N	Units
Impact Kinetic Energy	10	100	7	eV
ϕ_y	-90	180	4	degrees
ϕ_z	-90	90	2	degrees
Total			42	

C. Definition of Quantum Region

The quantum (QM) partition of the simulation cell is defined as the complete 24-atom EMI–BF₄ projectile and every subsequent fragmented species during the collision trajectory. By keeping all reactive bonds inside the QM region, the simulation avoids artificially linked atoms and suppresses charge leakage across the QM/MM boundary. The QM region is housed in a $25 \times 25 \times 25 \text{ \AA}^3$ GAPW box that is recentered on the instantaneous center of mass of the largest molecule after every MD step. This ensures a minimum of 5 Å buffer between any QM atom and the grid edge, thereby eliminating aliasing artifacts. Electronic interactions in the QM region are described with the GAPW implementation in CP2K³³. Each C, N, H, B, and F atom carries the aug-cc-pVTZ basis set. Its uncontracted Gaussian primitives are described in Equation 5

$$\chi_{\mu}(r_e) = \sum_{k_p} d_{\mu k_p} \left(\frac{\alpha_{k_p}}{\pi} \right)^{\frac{3}{4}} \exp(-\alpha_{k_p} |r_e - R_{\mu}|^2) \quad (5)$$

where $\chi_{\mu}(r_e)$ is the contracted Gaussian-type basis functions associated with atomic center μ and evaluated at the electron position r_e , the sum is evaluated over k_p for all primitive Gaussians that form the contraction, $d_{\mu k_p}$ represents the contraction coefficients, α_{k_p} are the primitive exponents, and R_{μ} represents the position vector of the nucleus on which basis function μ is centered. The aug-cc-pVTZ basis set supply both diffuse and polarization functions that are essential for capturing long-range charge transfer in ionic-liquid fragments³⁴. Exchange-correlation energies are evaluated with the ω B97x-V range-separated hybrid functional³⁵ with energy decomposition as given in Equation 6.

$$E_{XC} = aE_X^{HF,LR}(\omega) + (1-a)E_X^{GGA,LR}(\omega) + E_X^{GGA,SR}(\omega) + E_C^{GGA} + E_C^{NL} \quad (6)$$

where $E_X^{HF,LR}(\omega)$ is the long-range Hartree-Fock exchange evaluated with a range-separated Coulomb kernel set by ω , $E_X^{GGA,LR}(\omega)$ and $E_X^{GGA,SR}(\omega)$ are the long and short range components of the semilocal generalized gradient approximation (GGA) exchange, E_C^{GGA} is the semilocal GGA correlation, E_C^{NL} is the nonlocal correlation term such that the exact-exchange mixing coefficient $a = 0.167$ is supplemented by the rVV10 non-local dispersion kernel to recover London forces with plane-wave efficiency³⁶, and ω is the range-separation parameter controlling the long and short range partitions. Exact exchange integrals are accelerated by the Auxiliary Density Matrix Method (ADMM-Q), which reduces hybrid overhead by projecting onto a compact auxiliary basis set while retaining mE_h accuracy³⁷.

D. Definition of Classical Region

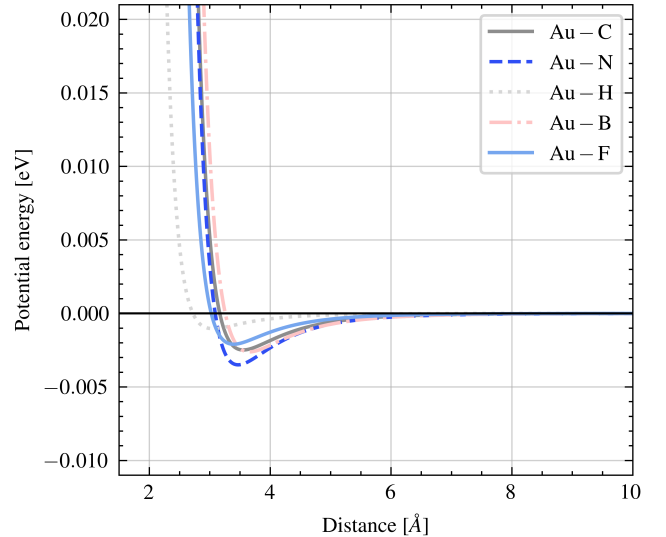


FIG. 5. Lennard-Jones pair potentials for short-range interactions between Au and QM atoms.

The classical (MM) partition represents a rigid Au extractor grid together with the $75 \times 75 \times 75 \text{ \AA}^3$ electrostatic vacuum beyond the QM box. Au-Au cohesion is described by the Foiles-Baskes-Daw EAM potential³⁸, the parameterization of which reproduces the lattice constant, cohesive energy, and elastic modulus of Au within experimental uncertainty. Because the collision energies examined here, 10 to 100 eV, are well below the sputtering threshold, the slab is held rigid to transit momentum accurately while preventing spurious hydrogen embedding. Pauli repulsion and dispersion between the QM fragments and surface atoms are captured through LJ cross terms as defined by Equation 7

$$U_{ij} = 4\epsilon_{ij} \left[\left(\frac{\sigma_{ij}}{r_{LJ}} \right)^{12} + \left(\frac{\sigma_{ij}}{r_{LJ}} \right)^6 \right] \quad (7)$$

which defines the 12-6 LJ potential applied to each Au-*j* pair, where r_{LJ} is the interatomic separation. Arithmetic mixing of Lennard-Jones parameters following the Lorentz-Berthelot rules^{39,40} is leveraged to calculate the well depths, ϵ , and cutoff parameters, σ for each Au-*j* pair using elementwise site values for N–N, C–C, H–H, B–B, and F–F⁴¹ as well as Au–Au⁴², as described in Equations 8 and 9.

$$\sigma_{ij} = \frac{\sigma_i + \sigma_j}{2} \quad (8)$$

$$\epsilon_{ij} = \sqrt{\epsilon_i \epsilon_j} \quad (9)$$

The well depths and cutoff parameters were calibrated to reproduce adhesion energies of EMI–BF₄ on Au and are depicted in Figure 5 and summarized in Table III.

TABLE III. Lennard-Jones well depths ϵ_{ij} and cutoff parameters σ_{ij} for non-bonded interactions between surface, Au, atoms and the constituent atoms of the EMI–BF₄ propellant.

Pair	ϵ_{ij} (eV)	σ_{ij} (Å)
Au-C	0.00249	3.167
Au-N	0.00350	3.092
Au-H	0.00104	2.722
Au-B	0.00262	3.258
Au-F	0.00210	3.0261

E. Fragmentation Criterion

Bond cleavage and formation is detected by tracking whether all atoms of the neutral ion cluster projectile remain connected throughout the microcanonical trajectory. At the k^{th} microcanonical frame, the instantaneous Cartesian position of atom *i* such that $1 \leq i \leq N$ is defined as $r_i^{(k)}$. Pairwise interatomic separations are computed using Equation 10.

$$d_{ij}^{(k)} = \| \mathbf{r}_i^{(k)} - \mathbf{r}_j^{(k)} \|, \quad 1 \leq i < j \leq N \quad (10)$$

These distances are converted into a bond connectivity matrix defined by Equation 11

$$A_{ij}^{(k)} = \begin{cases} 1, & d_{ij}^{(k)} \leq d_b, \\ 0, & \text{otherwise} \end{cases} \quad (11)$$

where a bond length threshold of $d_b = 5$ Å is selected. For each frame *k*, the connectivity matrix $A^{(k)}$ defines the undirected graph $G^{(k)} = (V, A^{(k)})$ with a vertex set $V = \{1, \dots, N\}$. Atoms are assigned to the same fragment when they are connected through at least one continuous path of pairwise connections. The number of disconnected groups in $G^{(k)}$, denoted

$C^{(k)}$, is interpreted as the fragment count at frame *k*. The microcanonical trajectory is treated as intact when $C^{(k)} = 1$. The fragmentation index k_{frag} is described in Equation 12

$$k_{\text{frag}} = \min (k > k_0 : C^{(k)} > 1) \quad (12)$$

which marks the first post-equilibration frame at which the neutral species has irreversibly split into two or more fragments.

F. Charge Analysis Protocol

Time-resolved atomic charges are extracted to quantify electron exchange between the projectile and its constituent atoms during impact. All charge analyses were performed with Multiwfn⁴³. Multiwfn is a wavefunction analyzer that supplies a variety of population analysis schemes. This study leverages the restrained electrostatic potential (RESP) model because it reproduces intermolecular electrostatics while damping excessive charge transfer on buried atoms⁴⁴. For each timestep, the partial charges $\{q_A\}$ are obtained by minimizing the RESP objective function described in Equation 13

$$\chi^2 = \sum_i w_i \left[V_i^{QM} - \sum_A \frac{q_A}{r_{Ai}} \right]^2 + \sum_A \lambda_A (q_A - q_A^0)^2 \quad (13)$$

where V_i^{QM} is the ab initio electrostatic potential at grid point *i*, w_i is the uniform weight (0.001 a.u.), r_{Ai} is the distance from atom *A* to point *i*, and the second term applies a hyperbolic restraint $\lambda_A = 5 \times 10^{-4}$ a.u. that prevents overpolarization. The grid spacing is fixed to 0.3 Å, and points lying within 1.4 Å of any atomic center are excluded.

Connectivity matrices generated from Section II E tag every atom with a fragment label *k*. The net charge of fragment *k* at time *t* is described by Equation 14. Charges are sampled every timestep from the moment of microcanonical ensemble initiation until 2 ps after impact.

$$Q_k(t) = \sum_{A \in k} q_A(t) \quad (14)$$

To map time-dependent RESP charges to integer charge states observed experimentally, fragments charges are binned using a small dead-band around 0 such that fragments with $Q_k(t) \leq -0.125e$ are labeled as anions, fragments with $Q_k(t) \geq +0.125e$ are labeled as cations, and fragments with $-0.125e \leq Q_k(t) \leq +0.125e$ are labeled as neutrals. This tolerance is intentionally larger than typical method, grid, and basis set dependent variability in partial atomic charges and avoids misclassifying weakly polarized fragments^{20,21,45}. To verify that the charge assignments are well-conditioned, Figure 6 reports the root mean square error (RMSE) and relative root mean square error (RRMSE) versus impact energy of the RESP fit. Both the absolute RMSE and RRMSE remain small

and weakly dependent across 10 to 100 eV, supporting the stability of the charge analysis.

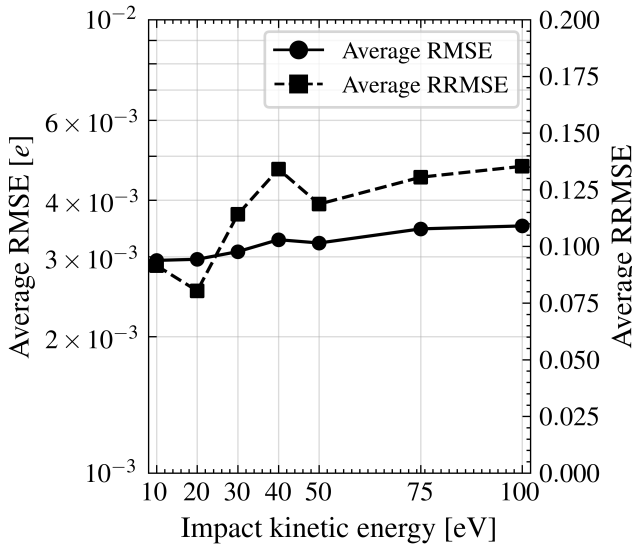


FIG. 6. Root mean square error and relative root mean square error averaged across impact energies derived from the RESP fit.

III. RESULTS

The surface collision ensemble reveals a clear progression of fragmentation pathways for neutral EMI–BF₄ projectiles colliding with an Au extractor surface across the 10 to 100 eV impact window. Figure 7 depicts the mass spectra colored by net fragment charge. Low energy collisions, 10 to 20 eV, are dominated by ionic dissociation of the neutral pair into the canonical IL constituents, the EMI⁺ cation and BF₄[−] anion. At intermediate energy, between 30 to 40 eV, the spectra develops strong neutralization channels, with prominent neutral products consistent with BF₃ and HF alongside a largely neutralized imidazolium backbone, C₆H₁₀N₂. Light charged fragments also appear, F[−] and BF₂⁺ within this impact energy regime for less than 25% of simulations. In the high energy regime, greater than 50 eV, the mass spectra distributions broaden substantially due to covalent fragmentation and become rich in light fragments with a mixture of neutral and charged products: CH₃⁺, CH₃[−], F[−], HF[−], C₂H₅⁺, BF⁺, CHBFN⁺, C₃H₃N₂[−], C₄H₆N₂⁺, BF₄[−], and C₅H₆N₂⁺ as summarized in Table IV. This energy-ordered sequence aligns with facility observations that surface collisions begin to emit electrons and charged molecular secondaries once the SEE and SIE limits of 0.44 eV/u and 1 eV/u¹⁹. The highest simulated energy of 100 eV places our surface impact simulations in the near-onset regime for secondary production at metallic targets, implying that this limit may be lower due to the number of charged species generated below this threshold. The net charges reported in Figure 7 rests on RESP-fitted partial charges computed at every MD timestep.

Figure 8 quantifies how the momentum and energy are par-

TABLE IV. Secondary ion species detected in the microcanonical QM/MM trajectories.

Mass (amu)	Species	Reference Detection
15	CH ₃ ⁺ , CH ₃ [−]	46, 47, 48
19	F [−]	49, 46, 47, 21
20	HF [−]	49, 46, 47, 21
29	C ₂ H ₅ ⁺	46, 47, 32, 21
30	BF ⁺	46, 32
49	BF ₂ ⁺	32
57	CHBFN ⁺	21
67	C ₃ H ₃ N ₂ [−]	32, 21, 48
81	C ₄ H ₅ N ₂ ⁺	48
87	BF ₄ [−]	49, 47, 32, 48
94	C ₅ H ₆ N ₂ ⁺	47, 48
111	C ₆ H ₁₁ N ₂ ⁺	46, 47, 32, 21, 48

titioned among these products by reporting the fraction of initial impact kinetic energy that each fragment carries after collision. At 10 to 20 eV, a small number of heavy fragments, most interestingly the transient metastable species C₆H₁₁N₂F and recombined neutral EMI–BF₄ pairs, carry most of the available kinetic energy. These outcomes are consistent with the ionic dissociation regime, where fragmented species dissipate less than half of the impact energy into the surface due to short-range Coulombic repulsion. Above 50 eV, covalent fragmentation becomes prevalent such that the impact energy is distributed over many light fragments. By increasing impact energy, the breakup transitions from few-body, energy-concentrated outcomes to many-body, energy-dispersed outcomes. This distinction is astutely important for ground tests where heavy fragments that retain a large fraction of the incident energy are more likely to deliver momentum to nearby hardware and to seed SEE or SIE. On the other hand, although the cloud of many light fragments distributes this energy broadly in the high energy impact regime, the light neutral fragments can initiate a cascade of fragmentation with heavier species that add to mass error in TOF measurements^{50–52}. Geiger et al. corroborates this finding through energy-swept Au target studies that report robust charged-secondary production from electrospray plume impacts across 30 to 1800 eV, that bound the upper window of this study.

Figure 9 represents the deflection angle distribution of fragmented species tracked in this study. The distribution peaks at moderate angles, 40 to 55° and exhibits a strong mass-to-angle anti-correlation such that heavier fragments preferentially scatter closer to the forward direction, while lighter fragments populate larger deflections. The scattering behavior is approximately Lambertian and dovetails with multiscale plume studies^{5,8,9} that tie beam interception to the number and distribution of active emission sites. From this distribution, it can be noted that heavy fragments increase grid and chamber interception probability, whereas light fragment scattering increases diffuse reflection contamination that directly correlates with facility effects.

The average fragment count logged during each simulation

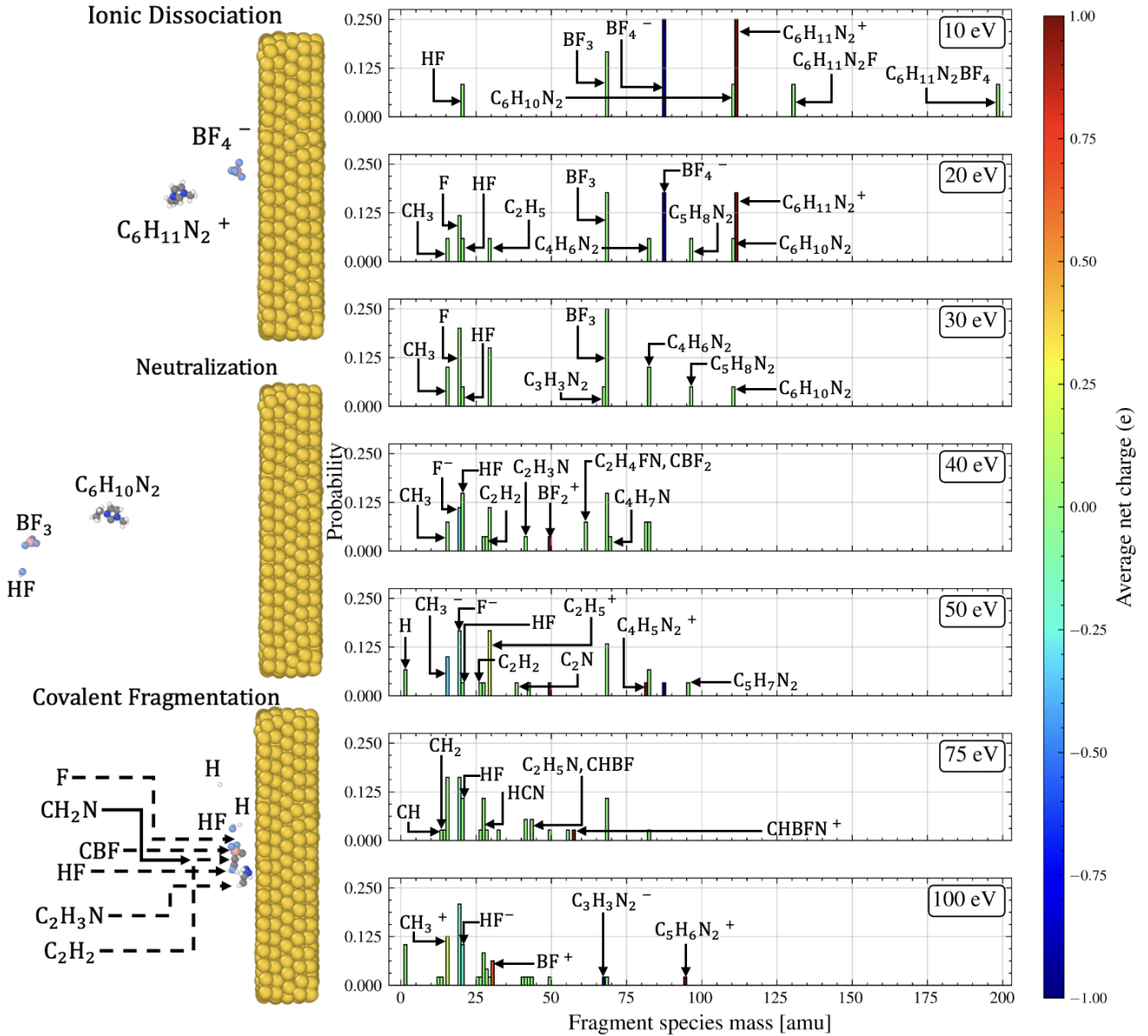


FIG. 7. Probability density of fragment species mass for impact kinetic energies from 10 to 100 eV.

rises monotonically as impact energy increases as described in Figure 10. The fraction of transient metastable fragments, which are species that are highly reactive and appear promptly after impact, peaks near 50 eV and declines at higher energies. This non-monotonicity is consistent with an intermediate energy neutralization window that readily forms volatile species such as CHBFN⁺ and neutrals such as HF. The appearance of neutral byproducts at intermediate energies connects directly with in-situ RGA in electrospray facilities¹⁸, which has identified neutrals and, most importantly, HF which is formed through: EMI–BF₄ → C₆H₁₀N₂ + BF₃ + HF.

IV. DISCUSSION

The atomistic picture that emerges from this study is a three-stage sequence with increasing impact energy: ionic dissociation of the neutral EMI–BF₄ pair in the low, 10 to 20 eV, regime, a neutralization window in the intermediate, 30 to 40 eV, regime characterized by BF₄⁻ → BF₃ + HF and a neutralized imidazolium backbone, C₆H₁₀N₂, and covalent fragmentation in the high, greater than 50 eV, regime that yields many light products with mixed charge states. Placing these regimes in the context of facility measurements clarifies why charged secondaries appear for nominally sub-threshold impacts. For a neutral EMI–BF₄ projectile, 100 eV corresponds to approximately 0.5 eV/u, falling right above the SEE onset of 0.44

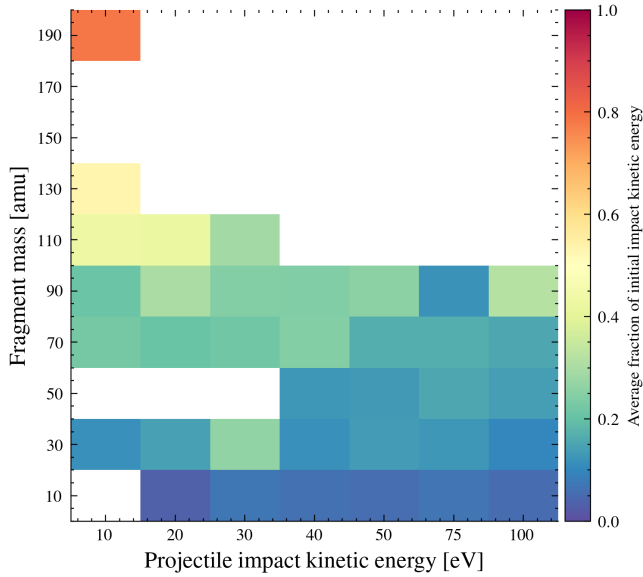


FIG. 8. Mass-resolved energy partition fraction as a function of initial projectile impact energy.

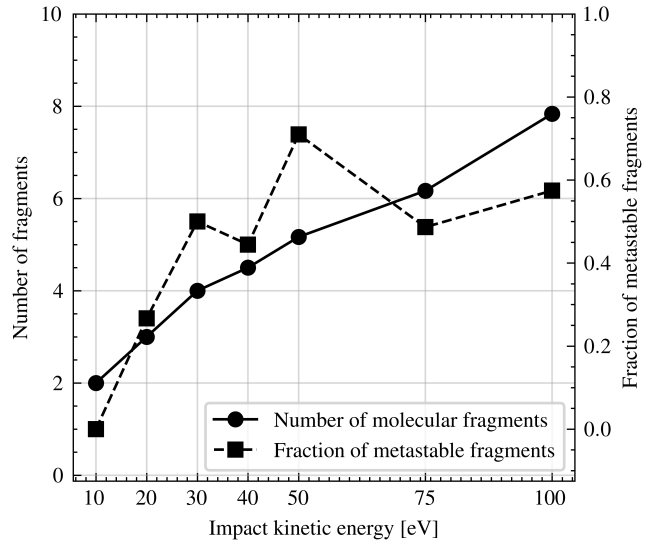


FIG. 10. Transient metastable species formation as a function of impact energy.

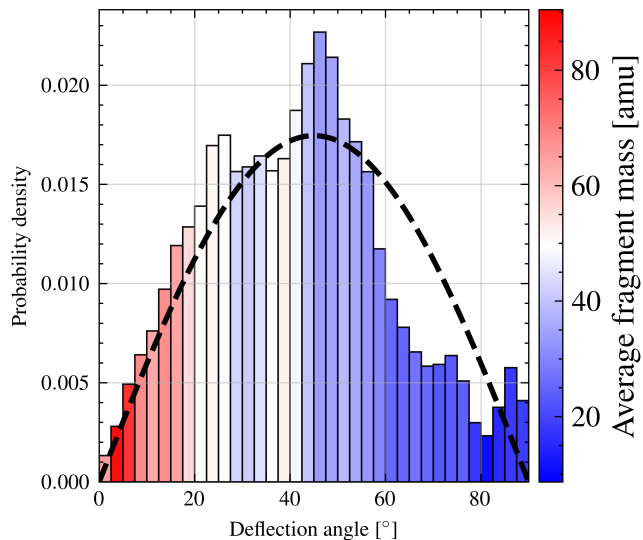


FIG. 9. Fragment mass deflection angle distribution averaged across all impact energies.

eV/u and below the SIE onset of $1\text{ eV}/u^{19}$. The trajectories described in this study therefore probe the near-onset regime where modest charge-secondary yields are expected and energetically plausible which is consistent with Uchizono.

A key operational implication from this work is that neutral fragments are not benign. The intermediate energy regime where neutralization is a dominant pathway coincides with abundant neutrals that scatter broadly. Geiger et al. justifies this behavior by describing that even when the ion portion of the plume is fully suppressed by a decelerating electrode, charged secondary species are still emitted from the target under neutral bombardment²⁰. The simulations presented in this

study provide evidence that charge redistribution within the projectile prior to or during impact produces charged fragments upon collision and underscore that neutral suppression in ground tests does not eliminate SSE near the source.

The pathways presented in this study clarify diagnostic behaviors in TOF-SIMS, suppression-bias probes, and QCM measurements. TOF-SIMS diagnostics record only charged secondaries whereas the data described in Section III predict the growth of specific charged fragments of CH_3^+ , CH_3^- , F^- , HF^+ , C_2H_5^+ , BF^+ , CHBFN^+ , $\text{C}_3\text{H}_3\text{N}_2^-$, $\text{C}_4\text{H}_6\text{N}_2^+$, BF_4^- , and $\text{C}_5\text{H}_6\text{N}_2^+$ with energy, while neutral channels of BF_3 , HF , and $\text{C}_6\text{H}_{10}\text{N}_2$ remain invisible to TOF. The neutral species characterized in this study must be captured with neutral diagnostics as demonstrated by Shaik et al. using RGA¹⁸. Suppression-bias probes have been established to recover positive and negative secondary current yields that enable correction of TOF and tandem energy-analyzer measurements⁵³. The results presented in this study indicate that these corrections are especially important once impacts reach the neutralization and covalent fragmentation regimes where light, large angle products are abundant. QCM measurements that transition from net deposition at low impact energies to sputter dominant response at higher energies are qualitatively consistent with the energy partitioning observed in this study. At low energies, few heavy fragments retain a large share of the energy, whereas at higher energy, the same budget is distributed across many light products.

At the plume scale, the anti-correlation between fragment mass and deflection angle recorded provides a bridge between single-impact chemistry and grid interception in arrays. Heavier fragments are biased to approximately specular reflection and, therefore, more likely to propel past extractor or accelerator hardware. Lighter fragments populate larger deflection angles, contributing to diffuse contamination that can contribute to mass error in experimental measurements^{50–52}.

Multiscale plume models that combine near-emitter physics with PIC transport have shown that the number and distribution of active emission sites steer beam divergence and interception^{11–13}. By folding the energy-dependent statistics into multiscale modeling frameworks, the ability to predict facility effects at the device level is possible.

The peak of transient metastables near 50 eV coincides with the onset of abundant neutral byproducts that are missed by traditional charged species diagnostics but are visible to RGA. The presence of these neutral byproducts can alter background chemistry and complicate long-duration characterization. Metastable intermediates make mass error characterization worse in single-emitter TOF measurements because prompt fragmentation and neutral formation between the source and detector reduce the charged-particle fraction sampled by TOF and retarding potential analysis (RPA). These complex surface processes bias inferred mass flow unless fragmentation models and neutral-species measurements are included. Future experimental work must develop tandem instruments that observe neutral and charged byproducts during EMI–BF₄ operation and controlled plume-surface impacts.

The trajectories presented in this work employ a QM/MM partition in which the projectile and its fragments are treated quantum-mechanically while the Au slab is classical and rigid. This model yields sufficient statistics across orientations and energies but does not allow explicit electron exchange with the metal or image-charge formation in the substrate. Therefore, fragment charges represent intra-fragment charge redistribution, and not metal-projectile electron transfer, and the conclusions made from this study are made in this context. Moreover, the 2 ps microcanonical ensemble window captures prompt chemistry and scattering but cannot access slower surface reconstruction, diffusion, or sputtering. Future modeling efforts should include polarizable or QM layers of the metal to capture image-charge and electron-transfer pathways, probe longer windows for thermalization and desorption, and couple per-impact statistics to plume-scale models to predict array-level divergence and interception. It is recommended that experimental measurements employ suppression-bias probes during TOF and RPA characterization by applying correction procedures to de-bias spectra from backstreamed secondaries. Furthermore, it is suggested to pair TOF with tandem RGA or direct neutral diagnostics to inventory neutral byproducts that dominate the intermediate impact window and perform energy-swept measurements across different target metals to anchor onset behavior. Implementing these efforts will improve the fidelity of performance measurements and extend hardware lifetime by managing SSE.

V. CONCLUSIONS

This work presents a comprehensive, atomistic investigation of neutral EMI–BF₄ surface collisions on Au extractor surfaces and implications for SSE and facility diagnostics in electrospray thrusters. Using energy-resolved QM/MM trajectories, we identify a three-stage sequence with increasing

impact energy, ionic dissociation between 10 to 20 eV, neutralization between 30 to 40 eV, and covalent fragmentation greater than 50 eV, and how to quantify how fragment composition, charge state, kinetic energy share, and scattering angle evolve across this window. The upper bound impacts at 100 eV correspond to $0.5 \text{ eV}/u$, falling right above the SEE onset and below the nominal SIE of $1 \text{ eV}/u$ which help explain the emergence of charged secondaries in the ground testing²⁰.

The trajectories confirm an operational point that neutral fragments pose danger to electrospray thrusters. In the intermediate energy regime, between 30 to 40 eV where neutralization pathways are dominant, large neutral populations with broad scattering angles are observed. Recent energy-swept Au target experiments using a decelerating electrode directly corroborate this simulated result by showing charged-secondary emission when the ion plume is fully suppressed²⁰. This demonstrates that neutral suppression alone does not eliminate SSE near the source, and, therefore, neutral management is needed.

The present QM/MM partition models the projectile and fragments quantum-mechanically and the Au classically, meaning that explicit electron exchange with the metal and image-charge formation are not captured. Future work should focus on extending this model to include polarizable or QM metal layers, longer time windows for thermalization and desorption, variation of target surfaces and IL projectiles, and coupling to multiscale plume transport that will enable quantitative forecasts of beam divergence, extractor impacts, and facility bias with uncertainty bounds. Future experimental efforts should focus on energy-resolved tandem neutral and ion measurements that can anchor onset behavior and calibrate neutral diagnostics in order to advance the physical understanding and measurement fidelity required for flight-relevant performance predictions.

ACKNOWLEDGMENTS

The authors would like to graciously acknowledge the support of the Air Force Office of Scientific Research Young Investigator Program under Dr. Justin Koo, Grant No. FA9550-23-1-0141.

AUTHOR CONTRIBUTIONS

Nicholas Laws: Conceptualization (lead); Data curation (lead); Formal analysis (lead); Investigation (lead); Methodology (lead); Software (lead); Validation (lead); Visualization (lead); Writing – original draft (lead); Writing – review & editing (lead).

Elaine Petro: Project administration (lead); Resources (lead); Supervision (lead); Writing – review & editing (supporting).

¹P. Lozano and M. Martinez-Sanchez, “Efficiency estimation of emi-bf4 ionic liquid electrospray thrusters,” in *41st AIAA/ASME/SAE/ASEE Joint Propulsion Conference & Exhibit* (2005) p. 4388.

²J. K. Ziener, "Performance of electrospray thrusters," in *31st International Electric Propulsion Conference* (2009) pp. 1–13.

³A. L. Collins, A. Thuppul, P. L. Wright, N. M. Uchizono, H. Huh, M. Davis, J. K. Ziener, N. R. Demmons, and R. E. Wirz, "Assessment of grid impingement for electrospray thruster lifetime," in *Proceedings of the 36th International Electric Propulsion Conference, Vienna, Austria* (2019) pp. 15–20.

⁴A. Thuppul, P. L. Wright, A. L. Collins, J. K. Ziener, and R. E. Wirz, "Lifetime considerations for electrospray thrusters," *Aerospace* **7**, 108 (2020).

⁵D. Krejci, F. Mier-Hicks, R. Thomas, T. Haag, and P. Lozano, "Emission characteristics of passively fed electrospray microthrusters with propellant reservoirs," *Journal of Spacecraft and Rockets* **54**, 447–458 (2017).

⁶P. Lozano and M. Martinez-Sanchez, "Ionic liquid ion sources: characterization of externally wetted emitters," *Journal of colloid and interface science* **282**, 415–421 (2005).

⁷X. Gallud and P. C. Lozano, "The emission properties, structure and stability of ionic liquid menisci undergoing electrically assisted ion evaporation," *Journal of Fluid Mechanics* **933**, A43 (2022).

⁸C. Ma and C. Ryan, "Plume particle energy analysis of an ionic liquid electrospray ion source with high emission density," *Journal of Applied Physics* **129** (2021).

⁹E. M. Petro, X. Gallud, S. K. Hampl, M. Schroeder, C. Geiger, and P. C. Lozano, "Multiscale modeling of electrospray ion emission," *Journal of Applied Physics* **131** (2022).

¹⁰O. Jia-Richards, "Quantification of ionic-liquid ion source beam composition from time-of-flight data," *Journal of Applied Physics* **132** (2022).

¹¹S. K. Hampl, M. T. Waggoner, X. Gallud Cidoncha, E. M. Petro, and P. C. Lozano, "Comparison of computational algorithms for simulating an electrospray plume with a n-body approach," *Journal of Electric Propulsion* **1**, 17 (2022).

¹²C. Whittaker and B. Jorns, "Modeling multi-site emission in porous electrosprays resulting from variable electric field and meniscus size," *Journal of Applied Physics* **134** (2023).

¹³A. G. Smith and E. M. Petro, "Propagating an electrospray emission model to array scales using particle-in-cell," *Journal of Propulsion and Power* **40**, 677–690 (2024).

¹⁴C. Guerra-Garcia, D. Krejci, and P. Lozano, "Spatial uniformity of the current emitted by an array of passively fed electrospray porous emitters," *Journal of Physics D: Applied Physics* **49**, 115503 (2016).

¹⁵M. R. Natisin and H. L. Zamora, "Performance of a fully conventionally machined liquid-ion electrospray thruster operated in pir," in *Proceedings of the 36th International Electric Propulsion Conference, Vienna, Austria* (2019) pp. 9–12.

¹⁶R. Bendimerad and E. Petro, "Molecular dynamics studies of ionic liquid-surface interactions for electrospray thrusters," *Journal of Electric Propulsion* **1**, 27 (2022).

¹⁷C. Geiger and E. Petro, "Qcm response to variable energy electrospray plume," *Journal of Electric Propulsion* **3**, 21 (2024).

¹⁸S. Z. Shaik, A. R. Bendimerad, A. T. M. Tahsin, A. Smith, P. Lozano, and E. Petro, "Characterization of propellant-surface collision byproducts using md simulations and rga measurements," in *AIAA SCITECH 2024 Forum* (2024) p. 1541.

¹⁹N. Uchizono, A. Collins, C. Marrese-Reading, S. Arestie, J. Ziener, and R. Wirz, "The role of secondary species emission in vacuum facility effects for electrospray thrusters," *Journal of Applied Physics* **130** (2021).

²⁰C. J. Geiger, G. Hofheins, and E. M. Petro, "Secondary species investigation of low energy electrospray plume impacts," *Journal of Electric Propulsion* **4**, 37 (2025).

²¹G. C. Hofheins, Z. Ulibarri, and E. M. Petro, "Electrospray propulsion time-of-flight secondary ion mass spectrometry diagnostic," *Review of Scientific Instruments* **96** (2025).

²²G. C. Hofheins and E. M. Petro, "Electrospray propulsion time-of-flight secondary ion mass spectrometry diagnostic," *39th International Electric Propulsion Conference* (2025).

²³N. Takahashi, "Molecular dynamics modeling of ionic liquids in electrospray propulsion," (2010).

²⁴F. Saiz and M. Gamero-Castaño, "Atomistic modeling of the sputtering of silicon by electrosprayed nanodroplets," *Journal of Applied Physics* **116** (2014).

²⁵A. P. Thompson, H. M. Aktulga, R. Berger, D. S. Bolintineanu, W. M. Brown, P. S. Crozier, P. J. In't Veld, A. Kohlmeyer, S. G. Moore, T. D. Nguyen, *et al.*, "Lammps-a flexible simulation tool for particle-based materials modeling at the atomic, meso, and continuum scales," *Computer physics communications* **271**, 108171 (2022).

²⁶X. G. Cidoncha, P. C. Lozano, R. Bendimerad, E. M. Petro, and S. K. Hampl, "Modeling and characterization of electrospray propellant-surface interactions," in *2022 IEEE Aerospace Conference (AERO)* (IEEE, 2022) pp. 1–11.

²⁷A. C. Van Duin, S. Dasgupta, F. Lorant, and W. A. Goddard, "Reaxff: a reactive force field for hydrocarbons," *The Journal of Physical Chemistry A* **105**, 9396–9409 (2001).

²⁸T. D. Kühne, M. Iannuzzi, M. Del Ben, V. V. Rybkin, P. Seewald, F. Stein, T. Laino, R. Z. Khaliullin, O. Schütt, F. Schiffmann, *et al.*, "Cp2k: An electronic structure and molecular dynamics software package-quickstep: Efficient and accurate electronic structure calculations," *The Journal of Chemical Physics* **152** (2020).

²⁹A. R. Choudhury, N. Winterton, A. Steiner, A. I. Cooper, and K. A. Johnson, "In situ crystallization of low-melting ionic liquids," *Journal of the American Chemical Society* **127**, 16792–16793 (2005).

³⁰D. Marx and J. Hutter, *Ab initio molecular dynamics: basic theory and advanced methods* (Cambridge University Press, 2009).

³¹G. J. Martyna and M. E. Tuckerman, "A reciprocal space based method for treating long range interactions in ab initio and force-field-based calculations in clusters," *The Journal of chemical physics* **110**, 2810 (1999).

³²S. Bell, A. T. M. Tahsin, and E. Petro, "Experimental study of collision-induced dissociation for emi-im and emi-bf₄," in *International Electric Propulsion Conference. Toulouse, France: Electric Rocket Propulsion Society* (2024).

³³J. VandeVondele, M. Krack, F. Mohamed, M. Parrinello, T. Chassaing, and J. Hutter, "Quickstep: Fast and accurate density functional calculations using a mixed gaussian and plane waves approach," *Computer Physics Communications* **167**, 103–128 (2005).

³⁴P. A. Hunt, "Quantum chemical modeling of hydrogen bonding in ionic liquids," *Ionic Liquids II*, 225–246 (2018).

³⁵N. Mardirossian and M. Head-Gordon, "wb97x-v: A 10-parameter, range-separated hybrid, generalized gradient approximation density functional with nonlocal correlation, designed by a survival-of-the-fittest strategy," *Physical Chemistry Chemical Physics* **16**, 9904–9924 (2014).

³⁶O. A. Vydrov and T. Van Voorhis, "Nonlocal van der waals density functional: The simpler the better," *The Journal of chemical physics* **133** (2010).

³⁷M. Guidon, J. Hutter, and J. VandeVondele, "Auxiliary density matrix methods for hartree-fock exchange calculations," *Journal of chemical theory and computation* **6**, 2348–2364 (2010).

³⁸S. Foiles, M. Baskes, and M. S. Daw, "Embedded-atom-method functions for the fcc metals cu, ag, au, ni, pd, pt, and their alloys," *Physical review B* **33**, 7983 (1986).

³⁹H. A. Lorentz, "Ueber die anwendung des satzes vom virial in der kinetischen theorie der gase," *Annalen der physik* **248**, 127–136 (1881).

⁴⁰D. Berthelot, "Sur le mélange des gaz," *Compt. Rendus* **126**, 15 (1898).

⁴¹J. De Andrade, E. S. Böes, and H. Stassen, "Computational study of room temperature molten salts composed by 1-alkyl-3-methylimidazolium cations force-field proposal and validation," *The journal of physical chemistry B* **106**, 13344–13351 (2002).

⁴²S. E. Huber, C. Warakulwit, J. Limtrakul, T. Tsukuda, and M. Probst, "Thermal stabilization of thin gold nanowires by surfactant-coating: a molecular dynamics study," *Nanoscale* **4**, 585–590 (2012).

⁴³T. Lu and F. Chen, "Multiwfn: A multifunctional wavefunction analyzer," *Journal of computational chemistry* **33**, 580–592 (2012).

⁴⁴C. I. Bayly, P. Cieplak, W. Cornell, and P. A. Kollman, "A well-behaved electrostatic potential based method using charge restraints for deriving atomic charges: the resp model," *The Journal of Physical Chemistry* **97**, 10269–10280 (1993).

⁴⁵D. J. Graham and L. J. Gamble, "Back to the basics of time-of-flight secondary ion mass spectrometry of bio-related samples. i. instrumentation and data collection," *Biointerfaces* **18** (2023).

⁴⁶J. Günster, O. Höft, S. Krischok, and R. Souda, "A time-of-flight secondary ion mass spectroscopy study of 1-ethyl-3-methylimidazolium bis (trifluoromethylsulfonyl) imide rt-ionic liquid," *Surface science* **602**, 3403–3407 (2008).

⁴⁷N. Bundaleski, S. Caporali, S. P. Chenakin, A. M. Moutinho, O. M.

Teodoro, and A. Tolstogouzov, "Ion-induced fragmentation of imidazolium ionic liquids: Tof-sims study," *International Journal of Mass Spectrometry* **353**, 19–25 (2013).

⁴⁸G. Hofheins, E. Petro, and A. Biedron, "Secondary species formed from ionic liquid electrospray ion plume impacts with propellant thin films," in *Proceedings of the 39th International Electric Propulsion Conference, London, England* (2025).

⁴⁹M. Van Stipdonk, V. Santiago, and E. Schweikert, "Negative secondary ion emission from nabf4: comparison of atomic and polyatomic projectiles at different impact energies," *Journal of mass spectrometry* **34**, 554–562 (1999).

⁵⁰C. T. Lyne, M. F. Liu, and J. L. Rovey, "A simple retarding-potential time-of-flight mass spectrometer for electrospray propulsion diagnostics," *Journal of Electric Propulsion* **2**, 13 (2023).

⁵¹M. R. Natisin, H. L. Zamora, Z. A. Holley, N. Ivan Arnold, W. A. McGehee, M. R. Holmes, and D. Eckhardt, "Efficiency mechanisms in porous-media electrospray thrusters," *Journal of propulsion and power* **37**, 650–659 (2021).

⁵²B. De Saavedra, D. Villegas-Prados, M. Wijnen, and J. Cruz, "Comparison between direct and indirect measurements for externally wetted electrospray thruster with adapted analytical balance," *Acta Astronautica* **232**, 283–295 (2025).

⁵³C. T. Lyne, M. F. Liu, and J. L. Rovey, "Quantifying secondary species emission from surfaces bombarded by an ionic liquid ion source," in *AIAA SCITECH 2024 Forum* (2024) p. 0689.

⁵⁴I. Martinez I Cano and K. D. Mease, "Electrospray propulsion performance for cubesat missions," in *AIAA SCITECH 2023 Forum* (2023) p. 2645.

⁵⁵M. Benetti, C. Colombo, C. Ryan, *et al.*, "Station-keeping with an electrospray propulsion system for low lunar polar mission on a 6u cubesat," in *INTERNATIONAL ASTRONAUTICAL CONGRESS: IAC PROCEEDINGS*, Vol. 13 (International Astronautical Federation, IAF, 2017) pp. 8937–8951.

⁵⁶A. Smith and E. Petro, "Array-scale modeling of electrospray ion plumes within afrl plume simulation tool turf," in *AIAA SCITECH 2023 Forum* (2023) p. 0063.

⁵⁷R. Bendimerad, N. Laws, and E. Petro, "Correction: Molecular dynamics studies of ionic liquid-surface interactions for electrospray thrusters," *Journal of Electric Propulsion* **3**, 24 (2024).

⁵⁸T. D. Kühne, *et. al.*, and J. Hutter, "Cp2k: An electronic structure and molecular dynamics software package - quickstep: Efficient and accurate electronic structure calculations," *The Journal of Chemical Physics* **152**, 194103 (2020), https://pubs.aip.org/aip/jcp/article-pdf/doi/10.1063/5.0007045/16718133/194103_1_online.pdf.

⁵⁹J. Adams, S. Foiles, and W. Wolfer, "Self-diffusion and impurity diffusion of fee metals using the five-frequency model and the embedded atom method," *Journal of Materials Research* **4**, 102–112 (1989).

⁶⁰O. Neunzig, P. Lozano, and M. Tajmar, "High-resolution direct thrust characterization of electrospray thrusters with emi-bf4 at different temperatures and polarities," *Journal of Electric Propulsion* **4**, 44 (2025).

⁶¹M. Schroeder, X. Gallud, E. Petro, O. Jia-Richards, and P. C. Lozano, "Inferring electrospray emission characteristics from molecular dynamics and simulated retarding potential analysis," *Journal of Applied Physics* **133** (2023).

⁶²G. B. Pipim, K. Sampson, J. Torres, N. Tingey, K. Flynn, D. Depew, J. Wang, and A. Krylov, "Ab initio simulations of dynamics of emi-bf4 ionic liquid propellant used in electrospray thrusters for nanosatellite applications," (2025).

⁶³A. T. M. Tahsin, A. R. Bendimerad, A. Smith, S. Thill, and E. Petro, "Cross-sections for charge exchange and other collisional processes in electrospray plumes," in *AIAA SCITECH 2024 Forum* (2024) p. 1540.

⁶⁴G. H. Takaoka, T. Hamaguchi, M. Takeuchi, and H. Ryuto, "Surface modification using ionic liquid ion beams," *Nuclear Instruments and Methods in Physics Research Section B: Beam Interactions with Materials and Atoms* **341**, 32–36 (2014).

⁶⁵S. Jhuree, M. S. Alexander, and J. P. Stark, "Electrostatic influence on charge to mass spectrum in mixed ion/droplet mode: implications for colloid thruster design," in *Proc. International Electric Propulsion Conference 2007* (2007).

⁶⁶Z. Ulibarri and E. Petro, "Direct two-dimensional goniometric steering of vacuum electrospray ion beams for angular time-of-flight studies," *Review of Scientific Instruments* **96** (2025).

⁶⁷S. Z. Shaik and P. C. Lozano, "Investigation of electrochemical gas generation in ion electrospray thrusters," (International Electric Propulsion Conference, 2024).

⁶⁸M. Naemura and Y. Takao, "Direct detection of neutral species from ionic liquid electrospray thrusters in the purely ionic regime," *Review of Scientific Instruments* **96** (2025).

⁶⁹E. E. Groopman, T. L. Williamson, and D. S. Simons, "Improved uranium particle analysis by sims using o 3- primary ions," *Journal of analytical atomic spectrometry* **37**, 2089–2102 (2022).

⁷⁰Z. Shen and S. Fearn, "Back-to-basics tutorial: Secondary ion mass spectrometry (sims) in ceramics," *Journal of Electroceramics* , 1–28 (2024).

⁷¹D. Schönenbach, F. Berg, M. Breckheimer, D. Hagenlocher, P. Schönberg, R. Haas, S. Amayri, and T. Reich, "Development, characterization, and first application of a resonant laser secondary neutral mass spectrometry setup for the research of plutonium in the context of long-term nuclear waste storage," *Analytical and Bioanalytical Chemistry* **413**, 3987–3997 (2021).

⁷²A. T. M. Tahsin, R. Bendimerad, A. Smith, S. Thill, N. Laws, and E. M. Petro, "Cross-sections for charge exchange and other collisional processes in electrospray plumes," *Journal of Propulsion and Power* , 1–11 (2025).

⁷³C. T. Lyne and J. L. Rovey, "Inferring ion cluster lifetimes from energy-resolved mass spectra of an emi-bf4 electrospray plume," *Journal of Applied Physics* **136** (2024).

⁷⁴E. M. Petro, X. Gallud, S. K. Hampl, M. Schroeder, C. Geiger, and P. C. Lozano, "Multiscale modeling of electrospray ion emission," *Journal of Applied Physics* **131**, 193301 (2022).

⁷⁵B. D. Prince, C. J. Annesley, R. Bemish, and S. Hunt, "Solvated ion cluster dissociation rates for ionic liquid electrospray propellants," in *AIAA Propulsion and Energy 2019 Forum* (2019) p. 4170.

⁷⁶C. J. Hogan and J. Fernandez de la Mora, "Ion-pair evaporation from ionic liquid clusters," *Journal of the American Society for Mass Spectrometry* **21**, 1382–1386 (2010).

⁷⁷C. E. Miller and P. C. Lozano, "Measurement of the dissociation rates of ion clusters in ionic liquid ion sources," *Applied Physics Letters* **116** (2020).

⁷⁸C. Chong, C. Maolin, and Z. Haohao, "Characterization of an ionic liquid electrospray thruster with a porous ceramic emitter," *Plasma Science and Technology* **22**, 094009 (2020).

⁷⁹N. Nuwal, V. A. Azevedo, M. R. Klosterman, S. Budaraju, D. A. Levin, and J. L. Rovey, "Multiscale modeling of fragmentation in an electrospray plume," *Journal of Applied Physics* **130** (2021).